



Full Text View

[Volume 29, Issue 3 \(March 1999\)](#)

Journal of Physical Oceanography

Article: pp. 480–499 | [Abstract](#) | [PDF \(1.06M\)](#)

Near-Surface Turbulence and Thermal Structure in a Wind-Driven Sea

Johannes R. Gemmrich*Institute of Ocean Sciences, Sidney, British Columbia, Canada, and University of Victoria, Victoria, British Columbia, Canada***David M. Farmer***Institute of Ocean Sciences, Sidney, British Columbia, Canada*

(Manuscript received April 16, 1997, in final form April 10, 1998)

DOI: 10.1175/1520-0485(1999)029<0480:NSTATS>2.0.CO;2

ABSTRACT

Ocean surface turbulence at high sea states is evaluated using heat as a naturally occurring passive tracer. A freely drifting instrument with a mechanically driven temperature profiler, fixed depth thermistors, and conductivity cells was used to monitor breaking wave activity and fine-scale temperature structure within the upper 2 m of the water column. The combination of temperature profiles and independent heat flux measurements demonstrate the presence of wave-enhanced turbulence and the effects of subsurface advection due to Langmuir circulation. The turbulence length scale, extracted from the temperature profile fine structure, suggests a surface value significantly smaller than previously reported. A Prandtl-type mixing length model matched with a surface energy flux due to wave breaking and the observed turbulent length scale is consistent with the authors' observations. Both advection and enhanced diffusion are reconciled in a two-dimensional model of the upper-ocean boundary layer, providing a framework for studying Langmuir circulation and upper-ocean turbulence in terms of the measured temperature structure.

1. Introduction

The exchange of momentum, heat, and gases between the atmosphere and ocean is strongly influenced by processes within the ocean surface layer. Very close to the surface, viscous and molecular sublayers of $O(1\text{ mm})$ prevail, but beyond this surface layer the transport is dominated by turbulent motions. The thermal molecular boundary layer, often called the cool skin ([Hasse 1971](#); [Katsaros 1980](#)), has attracted attention due to its significance to remote sensing ([Schlüssel et al. 1990](#)), but the turbulence beneath and its relation to breaking waves and

Table of Contents:

- [Introduction](#)
- [Observational approach](#)
- [Observations](#)
- [Discussion](#)
- [Conclusions](#)
- [REFERENCES](#)
- [FIGURES](#)

Options:

- [Create Reference](#)
- [Email this Article](#)
- [Add to MyArchive](#)
- [Search AMS Glossary](#)

Search CrossRef for:

- [Articles Citing This Article](#)

Search Google Scholar for:

- [Johannes R. Gemmrich](#)
- [David M. Farmer](#)


other features of the upper-ocean boundary layer are much less well understood. At moderate and high wind speed this near-surface turbulence is believed to play a significant role in air–sea gas exchange ([Kitaigorodskii 1984](#); [Woolf and Thorpe 1991](#)). In this report we discuss measurements of the near-surface ($z \lesssim 2$ m) temperature structure at relatively high sea states ($u_{10} \approx 13\text{--}17$ m s⁻¹) with frequent wave breaking and seek an interpretation in terms of wave-induced turbulence and Langmuir circulation.

Measurements of velocity fluctuations in the surface layer in Lake Ontario at significant wave heights of ~ 0.3 m ([Agrawal et al. 1992](#)) provided evidence of enhanced near-surface turbulence, attributed to breaking waves, previously indicated in wave tank measurements ([Rapp and Melville 1990](#)). Further support for elevated turbulence levels in the oceanic surface layer at wind speeds up to 13 m s⁻¹ was found by [Anis and Moum \(1992, 1995\)](#) with a turbulence shear probe and by [Drennan et al. \(1996\)](#) with velocity sensors. Combined turbulence and bubble cloud observations ([Osborn et al. 1992](#)) at wind speeds up to 9 m s⁻¹ indicate an important role of wave breaking and Langmuir circulation in the generation of enhanced near-surface turbulence levels. These observations however, did not reach into the most active layer within 0.5 m of the surface.


The observations described here were motivated by the recognition that, although direct measurements of the near-surface turbulence in the open ocean at higher sea states is extremely difficult, useful inferences might be gained from the somewhat less challenging measurement of temperature structure. Heat can serve as a passive tracer of the complex oceanic near-surface turbulence field and, if the air–sea heat flux is estimated independently, the temperature fine structure can be used to derive turbulent diffusivity and related properties.

Our dataset is limited to an 8-h period during night when wind mixing dominated convection. Despite the short duration of these observations, the sampling resolution and range of observational approaches provides an opportunity for testing models of near-surface turbulence. Specifically, we interpret the measurements with a Prandtl-type closure model combined with a prescribed energy input due to wave breaking. In this description we represent as a source of near-surface turbulence the short timescale processes associated with wind-driven shear and wave breaking, which normally last $\lesssim 30$ s, penetrate ~ 2 m below the surface, and are randomly distributed. Measurements of temperature anomalies in Langmuir convergence zones and bubble clouds allow further investigation of the link between wave enhanced turbulence and Langmuir circulation.

2. Observational approach

Our goal was to measure temperature profiles with high resolution over the upper 2 m of the ocean surface layer. For this purpose we modified a surface following sensor array previously developed for measuring wave breaking ([Farmer and Gemmrich 1996](#)). This instrument consisted of a lightweight vertical arm, with surface buoyancy connected by hinged supporting bars to the primary instrument housing ([Fig. 1](#) ). The instrument was tethered at 3-m depth in such a way as to ensure that the sensor arm pointed into the wind. The depth of the drogue is estimated at $O(30$ m). The drogue acted as a sea anchor that resulted in a slow drift of the instrument $\sim 65^\circ$ to the right of the wind direction. The spacing of the buoyancy at the top of the arm avoided disturbance to the surface layer at the sensor location. This arrangement allows unobstructed observation from an array that closely follows the undulating surface. Small but unavoidable displacements of the sensor arm relative to the surface were detected with a vertical capacitance wire gauge mounted close to the sensor arm, thus allowing reference of all data to the instantaneous sea surface.

The instrument is equipped with four conductivity cells; four Thermometrics FP07 fast-response thermistors (response time 7 ms in water) at depths of 0.12 m, 0.26 m, 0.36 m, and 0.51 m; and a SeaBird oceanographic thermometer SBE3 (response time 580 ms, typical drift of 4 mK yr⁻¹). The primary sensor was a thermistor (Thermometrics FP07) mounted on a small carriage fastened to a vertical wire passing over a pulley and driven by a stepping motor. The thermistor traversed the vertical arm once every 60 s at a speed of ~ 0.5 m s⁻¹. High temperature resolution of better than 1 mK was achieved by using the signal enhancement scheme described by [Mudge and Lueck \(1994\)](#). The thermometer at 1.8-m depth serves as a reference point for the profiling thermistor and small drifts of the fixed depth thermistors of order 1 mK h⁻¹ were adjusted by matching their values to the temperature profile. Surface elevations are estimated from the in-line acceleration of the sensor boom measured with a solid state accelerometer.

A second instrument designed to measure the spatial pattern of bubble distributions using acoustical backscatter was deployed in the same area ([Fig. 2](#) ). This instrument, which is supported at a depth of ~ 30 m by a rubber cord connected to a surface buoy, combines backscatter observations using vertically oriented narrow beam sonars (196 kHz, 400 kHz) with azimuthally scanning 100-kHz sonars for the detection of bubble cloud patterns ([Farmer and Li 1995](#)). The four independent azimuthally scanning sonars achieve a 360° image once every 30 s. The sonars can also operate in Doppler mode so as to obtain both the wave orbital components and the more persistent velocity field associated with Langmuir circulation. A recording thermistor attached to the rubber cord at 6.5-m depth provided an additional temperature measurement. Both instruments drifted freely, remaining between 1 and 6 km apart for the duration of the measurement

period.

Our observations were acquired west of Monterey, California ($36^{\circ}15'N$, $126^{\circ}26'W$) from the R/V *Wecoma* during the Marine Boundary Layer Experiment. The measurement period was 0010–0825 PDT 18 April 1995 following a rapid increase in wind speed from nearly calm conditions to a maximum wind speed of 17 m s^{-1} with steady direction from NNW (Fig. 3). Although this was a multi-investigator experiment with three vessels participating, the set of measurements acquired with the profiler during windy conditions were limited to the single deployment discussed here, during which the R/V *Wecoma* was unaccompanied.

Wave breaking was measured with conductivity sensors, as described by Farmer and Gemmrich (1996) and was intense throughout the deployment with mean periods between breaking events of $<30\text{ s}$. The air–sea temperature difference of roughly 2 K remained nearly unchanged throughout the deployment. There was no precipitation. Wind waves were developing under unlimited fetch conditions with significant wave height growing from 3 m to over 5 m . Calculation of the air–sea heat flux components and wind stress are based on the eddy correlation method and were performed by J. Edson who kindly made his calculations available to us. The heat flux within the thermal boundary layer increased from -150 to -350 W m^{-2} just before sunrise, mainly by latent heat loss due to evaporation. The Monin–Obukhov length was $O(-100\text{ m})$, indicating that despite strong surface heat loss, convection did not play a significant role in near-surface turbulence. Langmuir circulation developed within $\sim 1\text{ h}$ of the start of our measurements and well-organized bubble clouds were present during the remainder of the deployment (Fig. 4).

3. Observations

A segment of the temperature record at 1.8 m is shown in Fig. 5a. Superimposed on a cooling trend of approximately -40 mK h^{-1} are fluctuations of order 10 mK and a few minutes duration. As discussed below, we hypothesize that these short period decreases in temperature occur when the instrument drifts through successive Langmuir convergence zones. Surface water is cooled by the air–sea heat flux resulting in a deepening of the isotherms where it descends.

Previous field observations of the thermal structure of Langmuir circulation (Myer 1969; Thorpe and Hall 1982, 1987) show that under stable conditions, warmer water occurs on average within downwelling regions. Myer (1969) reported a temperature increase of more than 0.1 K beneath wind streaks for conditions in which surface water was up to 0.5 K warmer than at 7-m depth. Thorpe and Hall's (1982, 1987) measurements with a towed spar showed temperature fluctuations of $10\text{--}20\text{ mK}$ coincident with bubble clouds, although the temperature and sonar data were poorly correlated in detail. Our own observations of the bubble field, made with an upward looking sonar and the recording thermistor show moderately high correlation between the temperature at 6.5-m depth and the presence of deeply penetrating bubble clouds, which we ascribe to Langmuir convergence zones (Fig. 6). In this case, the positive heat flux leads to cooler water within convergence zones and warmer water between.

Bubbles are generated by breaking waves. However, the origin of near-surface bubble cloud variability is not unambiguously determined. Terrill and Melville (1997) attribute bubble cloud penetrations of $\sim 4\text{ m}$ to the direct injection of breaking waves, an interpretation supported by the coincidence of these events with the passage of wave groups. These injections lasted in the upper 1 m for periods of order 30 s and somewhat shorter at a few meters depth. On the other hand, examination of many sidescan records of the kind shown in Fig. 4, discussed in detail by Polonichko (1997), shows that there are long-lived bubble clouds, the properties of which cannot be directly attributed to breaking wave injection. For example, the larger structures in Fig. 4 typically persist for up to 25 min and have length scales of a few hundred meters. Similar persistent bubble clouds have been described by Thorpe (1984a, 1992) and Farmer and Li (1995). These are the dominant structures that appear to be associated with temperature fluctuations measured by the drifting sensor (Fig. 5).

a. Instrument drift and detection of Langmuir circulation convergence zones

Time series of the satellite-tracked instrument position, as well as visual observations, reveal that our instruments drifted according to the prevailing surface current at an angle of $\sim 65^{\circ}$ to the right of the wind direction (Fig. 2). The shear of the mean current also advected structures of the mixed layer such as Langmuir circulation relative to the sonar platform. This results in a southward displacement of these structures of $\sim 0.08\text{ m s}^{-1}$ estimated from the mean Doppler current in subsequent sonar images. Combining the relative drift components of the two instruments and the mixed layer we find that the surface drifter supporting the thermistors moved almost orthogonal to the orientation of the bubble clouds (Fig. 4), and hence the vertical array of thermistors at fixed depths monitors the horizontal temperature structure across Langmuir cells.

We may test the hypothesis that these events of anomalously low temperature occur within Langmuir convergence zones by comparing the spatial separation of bubble clouds measured with our sidescan imaging sonar with the corresponding spatial separation of measured temperature events. This is necessarily a stochastic comparison since the imaging sonar was

up to 6 km from the temperature sensor. Sonar sidescan images were collected with the acoustic platform every four hours for a one hour period starting at 0007 PDT. Drift paths of the two instruments are known from the satellite positioning, and a time series of drift velocities of the surface tracking float supporting thermistors relative to the drifting sonar instrument is calculated. Assuming individual sidescan images are representative of the prevailing bubble field, seven images selected from the beginning, middle, and end of each overlapping hour are chosen to simulate the instrument drift across the bubble field.

Repeated realizations of the instrument drift with random starting locations are obtained, and the time intervals between crossings of Langmuir convergences are recorded. Langmuir convergences are defined as locations with backscatter intensities above a threshold implying deviation from a normal distribution.

To extract the temporal separation of temperature fluctuations a time series is constructed of maximum temperature deviation between each point T_n and all data T_m within the previous 60 s, that is, $\Delta T_n = \min(T_n - T_m)$; $m = n - 120, \dots, n - 1$. Temperature events are defined as deviations ΔT exceeding a threshold of three standard deviations, and time and magnitude of each event are recorded. Temperature deviations corresponding to data shown in [Fig. 5a](#) are given in [Fig. 5b](#) along with detected temperature events.

[Figure 7](#) shows the distribution of periods between successive temperature events and the modeled encounters of Langmuir convergence zones along simulated drift paths within the sonar images. Although there are some discrepancies for the shortest and longest separation periods, the distributions of calculated and observed spacings are generally consistent. According to the Kolmogorov–Smirnov test the two distributions are the same at a 95% significance level, lending support to our interpretation of the temperature variability as an expression of the instrument’s passage through successive Langmuir convergence zones. Further support for this conclusion is provided by the correlation of the temperature record and bubble clouds ([Fig. 6](#)).

b. Variables describing Langmuir circulation

The width of Langmuir cells, defined as half the distance between adjacent bubble clouds seen in the sonar images, ranges from ~ 5 to ~ 50 m ([Fig. 8a](#)). Vertical velocities within Langmuir convergence zones, measured by upward looking sonars ([Farmer et al. 1997](#); [Polonichko 1997](#)) coinciding with our temperature measurements, vary from ~ 0.05 to ~ 0.12 m s^{-1} ([Fig. 8b](#)).

Temperatures at the five thermistors at fixed depths for the period identified in [Fig. 5a](#) are shown in [Fig. 9](#). Time series of the top four sensors have been lowpass filtered and resampled to match the 2-Hz sampling frequency of the deepest sensor. The temperature event appears at all five levels and has a duration of ~ 90 s. The mean instrument drift speed in the crosswind direction is 0.05 m s^{-1} , so that the observed traverse time corresponds to a convergence zone width of 4.5 m. The magnitude of the temperature deviation decreases with depth from ~ 17 mK at 0.12 m to 11 mK at 1.8 m.

Approximately 30% of breaking waves produce detectable temperature fluctuation $O(20\text{--}50$ mK) measured at the shallowest thermistor (0.12 m), but less than 1% of the events could be detected at the 0.26-m thermistor. These temperature anomalies occur when colder water from the surface layer is injected downward. The duration of temperature fluctuations associated with direct injection of surface water due to wave breaking is $O(1$ s) and the frequency of occurrence during this deployment is $O(60$ s). Hence, these events are distinct from advection within Langmuir circulation and turbulent diffusion between breaking events. The wave breaking temperature signal is dominated by the temperature of the water, despite the large air fraction within whitecaps ([Farmer and Gemmrich 1996](#)), which decreases rapidly with depth: Only 2.4% of breaking events are associated with air fractions greater than 0.01 at 0.26 m ([Gemmrich 1997](#)). These brief temperature fluctuations occur at times shown in [Fig. 5](#) but have been deleted from the temperature time series at 0.12-m depth in order to illustrate more clearly the passage of cool water associated with convergence zones.

Proceeding in this way, 119 events of anomalous low temperature were detected at 1.8 m. In each case the magnitude of the fluctuation was extracted at all five depths. Generally, the average magnitude of these fluctuations decreases more rapidly with depth than would be the case if surface water maintained its temperature as it descended, consistent with our expectation that mixing is occurring rather than simple overturning.

c. Temperature profiles

During the 8-h deployment a dataset of 414 temperature profiles was acquired. The profiles reach from 1.8-m depth to ~ 0.2 m above the interface and take about 4 s for one traverse. In order to avoid distortion of the measured temperature field by the profiling support, which is located below the thermistor, only upward profiles are utilized in the subsequent analysis. The profiling thermistor travels at a speed of 0.5 m s^{-1} and the temperature sampling rate of 34.375 Hz yield a spatial resolution of 14.4 mm. All depths are referenced to the instantaneous surface height recorded by the capacitance wire gauge. However, the separation of ~ 20 mm between the wire gauge and the profiler introduces an uncertainty in the depth

correction of up to 20 mm, depending on the slope of the water surface.

Individual profiles reveal the fine structure of the near-surface temperature field with fluctuations of up to 30 mK. Four representative profiles are shown in [Fig. 10](#). [A more extensive set of profiles can be found in [Gemmrich \(1997\)](#).] In the first profile, maximum deviations from the mean are less than 4 mK, whereas the third profile reveals a temperature inversion between 0.2-m and 0.4-m depth ~ 12 mK warmer than the mean and a second inversion of 5 mK lies between 1 m and 1.5 m.

The observed temperature fluctuations could arise from sources of water with anomalous temperature at the surface or below the mixed layer. The strong heat flux cools the water close to the ocean surface and subsequent mixing would result in temperature profiles similar to the observed profiles. The temperature deviation of the cool skin has a negligible heat content. A calculation based on the simple one-dimensional diffusion model discussed subsequently implies that a surface heat flux of -250 W m^{-2} would lead to a temperature difference of 35 mK between the surface and 40 m. Horizontal temperature fluctuations of order of 20 mK occurring over a distance of tens of meters are seen in temperature ramps and Langmuir circulation ([Thorpe 1995](#)) and hence horizontal advection may also play a role in the generation of the observed temperature fluctuations. CTD profiles acquired before and after the storm in the vicinity of the drifting sensors show a surface layer depth of 37 and 45 m, respectively. Water below this depth is ~ 0.2 K warmer than the overlying mixed layer and could serve as a source of measured near-surface temperature fluctuation.

Although the mean temperature profile, expressed as a deviation from the average in [Fig. 11](#), is not used in subsequent calculations, it clearly illustrates the negative mean gradient consistent with our expectations for an upward heat flux. The capacitance wire gauge is less precise during the high air fraction of a wave breaking event, resulting in a depth uncertainty of ~ 0.02 m. This affects values close to the surface. For comparison we also show an average profile from which the breaking events have been removed. Vertical gradients are greatest close to the surface, with or without the breaking wave profiles included. Within the top 0.1 m the temperature decreases by at least 8 mK. [Farmer and Gemmrich \(1996\)](#) hypothesized that in the presence of Langmuir circulation a thin surface layer $\sim O(10 \text{ mm})$ of anomalous temperature would exist, covering at least 30% of the surface. Although our sensor resolution is not fine enough to detect unambiguously such a layer, our present profiles are certainly consistent with this hypothesis. The ~ 1 mm thick cool skin is expected to exist on top of this boundary layer and except at locations of wave breaking ([Jessup 1996](#)) will always be present. The cool skin is negligible in terms of the analysis presented here.

4. Discussion

From our data analysis we find that the observed near-surface temperature structure can be interpreted in terms of a turbulent diffusion process, generated by wind stress and breaking waves, and advection due to Langmuir circulation. Laboratory experiments ([Rapp and Melville 1990](#)) showed that high turbulence levels introduced by wave breaking decay within approximately two wave periods, which yields for our conditions decay times of 20–30 s. [Terrill and Melville \(1997\)](#) further describe a large bubble cloud resulting from a nearby breaking wave that lasts $O(30 \text{ s})$. Maximum horizontal velocities in Langmuir circulation are $O(0.05 \text{ m s}^{-1})$ and cell widths are $O(10 \text{ m})$. Hence, the advection time along the sea surface between divergent and convergent zones for Langmuir circulation is of order 5 min and the advective timescale is at least one order of magnitude larger than the diffusive timescale associated with wave breaking and bubble injection.

We anticipate that the variability in surface bubble distributions arises from some combination of turbulence and advection associated with breaking waves and larger and more persistent advection associated with Langmuir circulation or similar larger scale structures. In seeking a simplification of this complex environment, we take advantage of the fact that the timescale of wave breaking effects is short compared to the timescale of Langmuir circulation. We therefore represent the combined effects of wave breaking, shear instability; and related short period phenomena near the surface, in terms of a depth dependent turbulent diffusivity.

For the small temperature fluctuations encountered, heat is essentially a passive tracer and the separation in timescales motivates an analysis based on separation of the advective and turbulent flow fields and an interpretation of the near-surface temperature fine structure in terms of the advection–diffusion equation:

$$\frac{\partial \theta}{\partial t} + \nabla \cdot (k_T \nabla \theta) - \tilde{V} \cdot \nabla \theta = 0, \quad (1)$$

where $\tilde{V} = (\tilde{u}, \tilde{v}, \tilde{w})$ describes the three-dimensional flow field, $\tilde{k}_T(z, t)$ is the thermal diffusivity, and $\tilde{\theta}$ is the potential temperature. The boundary conditions are a prescribed heat flux Q at the surface and a given temperature $\tilde{\theta}_0$ at the bottom of the mixed layer of depth H :

$$\frac{\partial \theta}{\partial \bar{z}} = \frac{Q}{\rho c_p k_T}, \quad \bar{z} = 0; \quad \theta = \theta_0, \quad \bar{z} = H. \quad (2)$$

The flow field can be specified based on observations and the air–sea heat flux is measured independently. The diffusivity profile $\bar{k}_T(z, t)$ describes the turbulence field. Direct calculation of the diffusivity field would require inversion of the advective diffusion model. Here we take an alternative approach, applying existing models for the diffusivity so as to compare results of the modeled temperature field with our observations.

a. One-dimensional analysis of temperature profiles

The vertical scale δz of fluctuations in the near-surface temperature profiles (Fig. 10) implies a scale of the turbulence elements with which they are associated. For the present purpose we define this scale as the distance between two successive temperature minima or maxima. Disturbances of 2 mK or less neighboring a larger disturbance are thought to be part of the larger structure and their size is added to the size of the larger fluctuation. The magnitude δT of the disturbance is taken as the maximum temperature difference within the part of the profile defining the disturbance.

In total, 977 disturbances fitted this definition. Their magnitudes and sizes were extracted and statistics obtained by applying the bootstrap method (Efron and Gong 1983). The magnitude of the temperature fluctuations is analyzed in more detail below, but we note here that the strongest fluctuations are observed close to the surface. If the water of anomalous temperature originated from below, the temperature fluctuations would be expected to decrease toward the surface, which is not the case in our dataset. We therefore infer that strong vertical near-surface temperature gradients are the most likely source of temperature fluctuations within the near-surface profiles. Our ability to determine the size of temperature disturbances is limited by the finite profiling depth. In the upper half of the profile, where the size estimate is not affected by the maximum profiler depth, a roughly linear increase of the size of turbulence elements with increasing depth can be seen (Fig. 12).

This increasing vertical extension of temperature fluctuations motivates a mixing length parameterization of the turbulence (Prandtl 1925), where the turbulent length scale, the so-called mixing length l_m , increases linearly with depth z and has a finite surface value mz_0 , where m is normally taken as the von Kármán constant:

$$l_m = m(z + z_0); (3)$$

z_0 is the roughness length. Although this concept is widely adopted in turbulence closure schemes (cf. Mellor and Yamada 1982), the need to include a surface length scale, which in general cannot be measured, introduces an arbitrariness to the application of such models. In the oceanic boundary layer the term *roughness length*, suggesting the presence of solid roughness elements, is misleading and in this context is more appropriately called the *surface mixing length*. A linear fit to the mean values obtained from the bootstrap method shown in Fig. 12 has a slope $m = 0.57$ and a surface mixing length $z_0 = 0.2$ m (solid line in Fig. 12). The regression coefficient is $r = 0.97$ and the uncertainty in surface mixing length is less than 0.04 m. As discussed subsequently, the inferred z_0 is much less than values suggested in the literature (Craig 1996; Drennan et al. 1996; Terray et al. 1996).

The slope m is greater than the von Kármán constant of $\kappa = 0.4$, which, however, falls well within the error bars. Nevertheless, there are physical factors that might account for the difference in the observed slope compared to the classical result for flow along a solid boundary. Close to the surface, buoyancy due to microbubbles can be expected to suppress the mixing length. With increasing depth the bubble concentration decreases, which would allow the eddy size to grow faster than in a homogeneous (stratified or unstratified) medium. At a certain depth, where the gradient in the stratification becomes sufficiently small, a slope of 0.4 will be approached. A second factor is that heat is more efficiently mixed than momentum, since κ/m can be interpreted as a turbulent Prandtl number Pr_t . Literature values of Pr_t are somewhat contradictory. However, in the absence of stratification $Pr_t \sim 1$, and $Pr_t < 1$ is expected only for unstable stratification (see, e.g., Kundu 1990). Hence, we favor the first explanation and shall use this mixing length result (3) with the assumption $Pr_t = 1$ and $m = 0.4$ in our subsequent discussion of the Craig and Banner (1994) model.

As discussed above, the thermal structure must be considered at least as a two-dimensional field to account for the effects of advection due to Langmuir circulation. However, it is useful to first consider a one-dimensional interpretation close to the surface, recognizing that even here the advective effects will to some extent modify the variables. We therefore define an *apparent* eddy diffusivity k_T , which is composed of a diffusive and an advective component:

$$k_T(z) = \frac{Q}{\rho c_p} \left(\frac{dT}{dz} \right)^{-1}. \quad (4)$$

If heat flux and temperature profile are known, k_T can readily be evaluated. This is done for all complete upward profiles, with the gradient estimated as temperature differences over 0.1 m and between 0.05-m and 0.1-m depth as the uppermost value. The heat flux is independent of depth since the profiles span only the uppermost 2 m and were all taken at night. No significant difference in the temperature field was observed during the short period of daylight observations ($\sim 0730\text{--}0830$ h), most likely because the shortwave flux was small ($<200 \text{ W m}^{-2}$) and the albedo due to low sun elevation was large. Nevertheless, profiles after 0730 PDT have been excluded from calculating k_T .

The apparent turbulent diffusivity profiles for measurements both within and between Langmuir convergence zones, which are identified by the low-frequency temperature fluctuations discussed above, are given in [Fig. 13](#). The apparent diffusivity increases by a factor of 10 within the top 1.6 m, with a near-surface value of roughly $2 \times 10^{-3} \text{ m}^2 \text{ s}^{-1}$. As water at the surface is advected by Langmuir circulation, it is exposed to the heat flux, and hence the greatest temperature anomalies are found within the upper part of the convergence regions. Since downwelling velocities are small near the surface, this yields large vertical gradients, and the apparent diffusivity is smallest in the near-surface region of the downwelling zones. Only 15% of the profiles were taken within ± 10 s of the instrument passing through the maximum of a temperature fluctuation, resulting in a wide scatter of the apparent diffusivity in convergence zones. Nevertheless, the general distribution of smaller apparent diffusivities in convergences can be seen. Furthermore, apparent diffusivities outside convergences are larger than predicted by constant shear stress, with increasing discrepancy closer to the surface. Consistent with our earlier assumption of scale separation we anticipate these differences in apparent diffusivity are due to advective effects rather than real differences in turbulence characteristics.

The turbulence models of Kolmogorov and Prandtl and Wieghardt (e.g., [Frost and Moulden 1977](#)) express the eddy diffusivity profile as

$$k_T(z) = u_t l_m = S_M q l_m, \quad (5)$$

where $l_m = m(z + z_0)$ is the mixing length and u_t specifies a turbulent velocity scale calculated from the equation for the turbulent kinetic energy $\frac{1}{2}q^2$:



$$\begin{aligned} \frac{1}{2} \frac{\partial q^2}{\partial t} - \frac{\partial}{\partial z} \left(l q S_q \frac{1}{2} \frac{\partial q^2}{\partial z} \right) \\ = l_m q S_M \left[\left(\frac{\partial u}{\partial z} \right)^2 + \left(\frac{\partial v}{\partial z} \right)^2 \right] - \frac{(q S_M)^3}{l_m}. \end{aligned} \quad (6)$$


Here, u , v are components of the mean horizontal shear flow and S_M , S_q are empirical constants. This widely used turbulence closure scheme was recently modified by [Craig and Banner \(1994\)](#) to incorporate wave enhanced near surface turbulence. The influence of wave breaking is imposed by a flux of turbulent kinetic energy through the surface, which, combined with a surface mixing length, defines the scale of the wave enhanced layer. We apply this model to calculate the eddy diffusivity (5) for comparison with our observations. The mixing length l_m is defined by our observed scale of vertical temperature fluctuations. However, the constants $(S_M, S_q) = (0.39, 0.2)$ were taken from [Craig and Banner \(1994\)](#). The value of S_M depends on stratification ([Mellor and Yamada 1982](#)). In our case the flux Richardson number R_F in the upper few meters is rather small, $-0.02 < R_F < 0$, and stability introduced modifications of S_M are less than 1% and hence not considered. We test the validity of the model and in particular the choice of S_M . The original model formulation prescribes the surface flux of the turbulent kinetic energy to be proportional to the cube of the friction velocity in water $E = \alpha u_*^3$, with a wave factor $\alpha = 100$. However, we use


$$E_{in} = \bar{c}_p u_*^2, \quad (7)$$

where u_* is the friction velocity in water and $\bar{c}_p = 0.8 \text{ m s}^{-1}$ is the effective phase speed of waves acquiring energy from

the wind ([Gemrich et al. 1994](#)), which accounts for the fact that energy from the wind enters the ocean surface layer via the wave field. For the mean friction velocity during this deployment ([7](#)) yields approximately half of the energy input assumed by [Craig and Banner \(1994\)](#).

Near-surface turbulence in this model is very sensitive to the choice of surface mixing length and the ad hoc formulation of this closure parameter is rather arbitrary. However, the analysis of the temperature profiles provides an estimate of $z_0 = 0.2$ m. A further estimate of z_0 can be obtained by comparison of the modeled diffusivity profiles with the diffusivities inferred from the temperature profiles. As pointed out earlier, turbulence is assumed to be unaffected by Langmuir circulation, yet the temperature field is composed of a diffusive and an advective component and a one-dimensional interpretation of our measurements can only yield an apparent eddy diffusivity. Therefore, a valid comparison has to either remove the advective component from the measured data or include advection in the model. In order to account for advection, the near-surface temperature field is computed with the steady-state advection–diffusion model, described below, from which the apparent model diffusivity is calculated according to ([4](#)). The advective diffusion model was run for representative model parameters ([Fig. 8](#) , [Fig. 14](#) ) and a mean profile of the apparent diffusivity is calculated as the average of all model realizations and averaged across one cell. The calculation is repeated for different input diffusivity profiles, relating to various surface mixing lengths.


Based on our analysis of the temperature profiles we vary the surface mixing lengths from 0.1 to 0.4 m and for comparison include the result for $z_0 = 4.5$ m, which is the mean value of the significant wave height ([Fig. 15](#) ). Again, the observations, that is, the mean of all diffusivity profiles between 0200 and 0800 PDT, exhibit a wave-enhanced surface layer with diffusivities up to 20 times larger than wall layer scaling predicts. This feature is also well captured by the [Craig and Banner \(1994\)](#) model diffusivities. A surface mixing length of 0.2 m provides the least mean relative error and smallest mean absolute error between apparent model diffusivities and our observations. This result is consistent with the surface mixing length $z_0 = 0.2$ m derived from the fluctuations of the measured temperature profiles. For this surface mixing length the advective component is insignificant in the upper 0.5 m; however, at the bottom of the profile the apparent diffusivity is roughly twice as large as would be the case if no advection was present. Had we assumed a turbulent Prandtl number $Pr_t = 0.8$ ([Mellor and Yamada 1982](#)), modeled diffusivities would be 20% smaller and the model would agree with our observations for a surface mixing length $z_0 = 0.25$ m. [Craig and Banner's \(1994\)](#) original estimate of the energy input would require a surface mixing length of ~ 0.15 m in order to match the observed diffusivity profile.

If it is accepted that the near-surface enhanced turbulence is generated by breaking waves, the length scale of this turbulence has to be related to the wave properties. [Craig and Banner \(1994\)](#) suggest the surface mixing length is comparable to the wave amplitude and find reasonable agreement with dissipation measurements by [Agrawal et al. \(1992\)](#) and [Osborn et al. \(1992\)](#) for z_0 between 0.1 and 1 m. [Drennan et al. \(1996\)](#) specify a surface mixing length in the range 1–3 m for the model to be in accordance with their dissipation measurements at significant wave heights between 0.9 and 2.6 m. Analyzing wave tank data [Craig \(1996\)](#) concludes tentatively that the magnitude of the surface mixing length is approximately one-sixth of the wavelength, or roughly the inverse of the wavenumber. Even by accounting for the size of breaking waves being less than the size of the dominant wave, these estimates predict a surface mixing length of several meters. Such a large value of surface mixing length implies diffusivities at least one order of magnitude larger than we observe ([Fig. 15](#) ).

By analogy with grid stirred turbulence where z_0 represents the stroke of the grid, the surface mixing length might be interpreted as the size of the initially stirred surface layer. Our conductivity measurements show that high air fractions in breaking waves are rarely entrained to the depth of the second conductivity sensor at 0.26 m, but air fractions of order 0.5 are commonly observed at 0.12 m. The above specified surface mixing length of $z_0 = 0.2$ m is consistent with the depth of air entrainment beneath breaking waves.

We therefore conclude that with a surface mixing length of 0.2 m and a surface energy flux $E_{in} = \bar{c}_p u_*^2$, the [Craig and Banner \(1994\)](#) model provides a reasonable description of the diffusivity profile.

1) GENERATION OF TEMPERATURE FINE STRUCTURE

Several processes of various scales relevant to near-surface temperature fine structure have been identified and are sketched in [Fig. 16](#) . In the upper few meters of the mixed layer of depth z_{ML} turbulence levels are significantly larger than expected in a constant stress layer, due to direct input of the turbulent kinetic energy via wave breaking. Commonly, direct air entrainment (air fractions ≥ 0.01) in spilling breaking waves is mainly restricted to the upper ~ 0.2 m, which coincides with the apparent surface value of the mixing length z_0 . This length scale does not describe the depth of the layer influenced by wave breaking. [Rapp and Melville \(1990\)](#) observed in the laboratory that breaking waves mix dye to 2–3 wave

heights within five wave periods of the breaking. It is hypothesized that advection of surface water into Langmuir convergences combined with strong air–sea heat fluxes generate a thermal boundary layer z_T of $O(20\text{--}50\text{ mK})$ a few centimeters thick. We emphasize that the near-surface temperature is expected to be highly variable so that a simple, well-defined layer is not implied.

A simple model of heat diffusing from the thin surface layer z_T into the water column can now be constructed and the results compared with the observed magnitude of temperature fluctuations. This allows a further comparison of the [Craig and Banner \(1994\)](#) model with our data. Turbulent motion, caused by wave breaking and shear-driven overturns, transport surface water of anomalous temperature downwards in the water column and its temperature equilibrates to the ambient temperature according to Newton’s law of cooling:

$$\frac{dT}{dt} = \frac{k_T}{A}(T - T_0) \quad (8)$$

where T_0 is the initial temperature anomaly and A is the surface area of the volume of water of anomalous temperature, assumed spherical in this highly idealized representation. This volume of water is transported by turbulent eddies downward where both the diffusivity and the volume increase so that $k_T(z) = S_M q m(z + z_0)$ and $A(z) = \pi[m(z + z_0)]^2$. The solution of [\(8\)](#) is

$$\begin{aligned} T(z(t)) &= \int_0^\tau T_0 \exp\left\{\frac{-tk_T}{A}\right\} dt, \\ z(t) &= 2\pi^{-1} \int_0^\tau q dt, \end{aligned} \quad (9)$$

which describes the magnitude of the temperature fluctuation as a function of depth.

Since the modeled temperature anomalies are a strong function of the empirical constant S_M , a comparison between observations and model provides a further test of the choice of S_M . This comparison is shown in [Fig. 17](#). The mean value of the temperature fluctuation decreases from 11 mK at depth 0.1 m to 5 mK at 1.5 m. Maximum values close to the surface are about 30 mK, but only 10 mK at the bottom of the profile. Modeled temperature fluctuations are shown for four choices of S_M . A good agreement with the observations is achieved for $S_M = 0.39$, the value suggested by [Craig and Banner \(1994\)](#). Varying this value by $\pm 30\%$ ($S_M = 0.27$ and $S_M = 0.51$) provides bounds for our measurements, but elimination of this empirical constant ($S_M = 1$) would generate a very rapid decrease of temperature anomalies which is not supported by our data.

The energy dissipation $\epsilon(z)$ in the turbulence model is specified by

$$\epsilon(z) = \frac{(S_M q)^3}{l_m} = \frac{k_T^3}{l_m^4}. \quad (10)$$

Dissipation rates fall off very rapidly with depth. Approximately 88% of the total dissipation occurs within the upper two meters. Enhanced dissipation rates $\epsilon/(u_*^3/\kappa z) > 1$ are predicted in the upper 1 m, with a maximum enhancement of close to ten times the dissipation in a constant stress layer. The enhanced turbulence in the model occurs at nondimensional depths gz/u_*^2 one to two magnitudes smaller than reported by other investigators (cf. [Anis and Moum 1995](#)). We conclude, in agreement with [Agrawal et al. \(1992\)](#), that this constant stress layer normalization of depth and dissipation rates is not applicable in this environment. The turbulent kinetic energy input through the wave field accounts for 88% of the total dissipation D occurring in the mixed layer of depth H_{ML} :

$$D = \int_0^{H_{ML}} \epsilon(z) dz. \quad (11)$$

This is consistent with the assumption that breaking waves are the major energy source in the surface layer.

b. Two-dimensional analysis: Inclusion of Langmuir circulation

Subsequent interpretation of the temperature structure within Langmuir circulation requires a description of the corresponding flow field. As a first estimate the advective field may be approximated by two counterrotating circular flow patterns (Thorpe 1984a) defined by the streamfunction ψ :

$$\begin{aligned} u &= -\frac{\partial\psi}{\partial z}; & w &= \frac{\partial\psi}{\partial x} \\ \psi &= u_0 \sin(\pi x') \sin(\pi z/\gamma) \\ x' &= \begin{cases} \frac{1 - |x|}{2 - 2\alpha} & \text{for } |x| \geq \alpha \\ \frac{|x|}{2\alpha} & \text{for } |x| < \alpha. \end{cases} \end{aligned} \quad (12)$$

Here the horizontal and vertical coordinates x and z are normalized by the width L of one cell so that the domain is given by $x = \pm 1$ and $z = 0, z = \gamma$, where γ is the cell aspect ratio. The inclusion of the asymmetry factor $0 < \alpha < 1$, which determines the center of the cell, allows for a difference in the strength of upwelling and downwelling, and u_0 defines the maximum downwelling velocity. Hence, the flow pattern is set by four parameters: L and γ define the geometry of the cell and α and u_0 specify the strength of the circulation. Cell width and downwelling velocity can be evaluated utilizing the acoustical observations (Fig. 8). No measurements of the deeper flow field were acquired in this experiment. However, such observations were acquired in an earlier study under somewhat similar conditions, using neutrally buoyant mixed layer floats (D'Asaro and Dairiki 1997), which serve as Lagrangian tracer. We used either three or four GPS-tracked surface floats with acoustical positioning to determine the location of the neutrally buoyant floats, permitting calculations of the parameters α, γ . The neutrally buoyant float measurements were acquired on 17 January 1995 off the coast of Oregon when well-developed Langmuir circulation was observed. Wind speed, wave field, and estimated buoyancy flux were similar during the two datasets; however, the mixed layer depth of ~ 70 m exceeded the 45-m mixed layer depth of the experiment described here. We assume similarity of the flow pattern of Langmuir circulation and evaluate α, γ from this dataset. Therefore, we define a cell as the float track between two successive surface approaches to within 4 m and a descent to a minimum of 10 m in between. The cell aspect ratio γ is the ratio of maximum depth to maximum crosswind displacement and the asymmetry of maximum upwelling and downwelling speed define α . (Fig. 14).

Individual larger windrows can be traced for up to 30 min on successive sonar sidescan images, a time long enough compared to the time needed for the surface water to be advected into the downwelling region. We therefore eliminate the time dependence in (1) and incorporate the diffusivity profile specified above in (1), (2) to calculate a mean steady state temperature field. While it is recognized that the pattern of Langmuir circulation includes three-dimensional features (Farmer and Li 1995), the basic structure is that of counterrotating parallel vortices. Therefore, the model will be reduced to a two-dimensional description of the temperature field, and the representative circulation given by (12) is assumed.

The horizontal coordinate x is perpendicular to the direction of the windrow and the second coordinate z is vertical, positive upward. The equations are nondimensionalized in the following way:

$$\begin{aligned} x &= \frac{\tilde{x}}{L}, & \theta &= \frac{\theta \rho c_p \tilde{\kappa}_T(\gamma L)}{QL}, \\ \mathbf{U} &= \frac{\tilde{\mathbf{U}}L}{\tilde{\kappa}_T(\gamma L)}, & \kappa_T(z) &= \frac{\tilde{\kappa}_T(z)}{\tilde{\kappa}_T(\gamma L)}, \end{aligned} \quad (13)$$

where L, γ are cell width and cell aspect ratio, respectively, and $\tilde{\mathbf{U}} = (\tilde{\mathbf{u}}, \tilde{\mathbf{w}})$ describes the two-dimensional flow field.

After applying this nondimensionalization and neglecting time dependence the model is given by

$$\nabla_h \cdot (k_T \nabla_h \theta) - \mathbf{U} \cdot \nabla_h \theta = 0, (14)$$

where $\nabla_h = (\partial/\partial x, \partial/\partial z)$, with boundary conditions

$$\begin{aligned} \frac{\partial \theta}{\partial z} &= \frac{1}{k_T}, & z = 0; & & \theta = 0, & & z = \gamma, \\ \frac{\partial \theta}{\partial x} &= 0, & x = \pm 1. & & & & \end{aligned} \quad (15)$$

The velocity field $\mathbf{U} = (u, w)$ is described by (12), subject to observed values of cell width, cell aspect ratio, flow asymmetry, and maximum flow speed. The diffusivity profile $k_T(z)$ is prescribed in accordance with the observed vertical structure of the temperature field, but comparison with other diffusivity profiles in the literature is also made.

Figure 18 shows an example of the modeled temperature and velocity field. As water reaches the surface in the upwelling region it is exposed to the air-sea heat flux, generating a thermal boundary layer. Since heat acts as a passive tracer, the thermal boundary layer thickens and intensifies in the convergence region as water of anomalous temperature accumulates and is drawn down. Diffusion, which increases with depth, diminishes local temperature gradients, leaving the lower part of the cell and the upwelling region nearly isothermal. In the case of surface heat loss this results in a tongue of cold water centered around the maximum downwelling. The model does not include potential entrainment at the bottom of the cell. However, if entrainment of water occurred, we expect temperature gradients to be erased by strong diffusion and the near-surface temperature structure not to be significantly different from the present case.

Li and Garrett (1995) show the temperature θ at any given point results from a combination of heat advection and diffusion and can be split into a conduction reference temperature θ_d and the perturbation temperature θ' due to advection, $\theta = \theta_d + \theta'$. The magnitude of the perturbation temperature, and hence the advective component of the apparent diffusivity, is a function of cell geometry and flow strength and varies with the relative position within the Langmuir cell. In the convergence region the advection of heat causes the largest vertical gradients, which results in the smallest apparent diffusivities $k_T = (dT/dz)^{-1}$, with a 30% increase at 2 m over the truly diffusive reference stage. This amplification increases to 150% in the divergence zone. Closer to the surface, where vertical velocities are small, the contrast between upwelling and downwelling regions decreases, with fairly uniform apparent diffusivities above 1-m depth.

In order to evaluate different diffusivity parameterizations, we calculate a set of approximately 800 temperature fields, utilizing the range of observed Langmuir circulation model parameters (Fig. 8, Fig. 14). The calculations are carried out using three different diffusivity profiles corresponding to (i) the wave-enhanced near-surface layer model discussed above, (ii) a constant diffusivity $k_T = 2.6 \times 10^{-5} u_{10}^3 g^{-1}$ suggested in Li and Garrett (1995), where u_{10} is the wind speed at 10-m height and g is gravitational acceleration, and (iii) constant stress layer scaling $k_T = u_* \kappa z$.

With each model solution we determine the horizontal temperature difference between downwelling and upwelling as a function of depth:

$$\Delta T_h(z) = T(z, 0) - T(z, 1). (16)$$

This parameter is evaluated at the six mean sensor depths (0.12 m, 0.26 m, 0.36 m, 0.51 m, 1.8 m, and 6.5 m) and compared with observed temperature fluctuations associated with Langmuir convergence zones for each of the models.

Figure 19 shows the distribution of $\Delta T_h(z_i)$ for the Craig and Banner (1994) model with $z_0 = 0.2$ m. The model calculations show some consistency with the observations. Generally, observations have a slightly narrower distribution than the model. They are best reconciled at 6.5-m depth, where the median values of observations and model agree within 1%. The largest discrepancy of 20% occurs at 1.8 m; the overprediction is 14% at 0.51 m, 2% at 0.36 m, 4% at 0.26-m depth, and 8% at the shallowest sensor. Nevertheless, the model appears to reproduce the overall depth dependence of the horizontal gradient, with the median value close to the surface being 2.4 times the median value at 6.5-m depth.

The predicted vertical profile of ΔT_h is sensitively dependent on the model choice. Figure 20 shows $\Delta T_h(z)$ for each of the three models with the three different diffusivity profiles shown on the right. The figure shows profiles for representative

values, $L = 20$ m, $\gamma = 1.4$, $\alpha = 0.4$, $u_0 = 0.08$ m s⁻¹. For each model the shape of $\Delta T_h(z)$ is relatively consistent through the range of Langmuir circulation parameters. Calculations using constant stress layer scaling, for which k_T is strongly suppressed close to the surface, yield large near-surface temperature anomalies. In the lower half of the cell $\Delta T_h(z)$ closely follows the profile of the wave enhanced case. The constant diffusivity model predicts much higher $\Delta T_h(z)$ than the wave-enhanced case, except in the upper 1 m, where they coincide and diffusivities of the two models are comparable. The constant diffusivity profile shows little depth dependence in $\Delta T_h(z)$. Far the best fit to the observations is predicted by the wave-enhanced model.

5. Conclusions

Heat can serve as a passive tracer of the complex oceanic near-surface turbulence field created by breaking waves, shear stress, and the advective field of Langmuir circulation. In a steady state description, averaged over several Langmuir circulation cycles, an ~ 2 m thick near-surface layer of enhanced turbulence in the open ocean in storm conditions was identified and linked to breaking wave activity. Our findings are consistent with results of previous studies ([Agrawal et al. 1992](#); [Anis and Moum 1992, 1995](#)) and provide further evidence that the concept of enhanced turbulence levels is applicable to open ocean storm conditions with typical significant wave heights of order 5 m.

The turbulent length scale z_0 can be estimated from the fine structure of measured temperature profiles. In our observations z_0 is found to have a surface value of ~ 0.2 m, increasing approximately linearly with depth. These observations support a mixing-length-type turbulence closure model. The mean diffusivity profile is well represented by [Craig and Banner's \(1994\)](#) modification of a conventional turbulence model in which we included an improved parameterization of the wave energy input ([Gemmrich et al. 1994](#)). The best fit of the model surface mixing length of $z_0 = 0.2$ m is essentially identical to our independent estimate of z_0 from overturning scales in the measured temperature profiles. This surface mixing length is also comparable to the vertical scale of air entrainment in whitecaps.

Beside the surface mixing length the turbulence model contains two rather arbitrary empirical constants S_M , S_q . The value of S_M could be tested by comparing a modeled temperature fine structure and the observed structure and the best agreement was found for $S_M = 0.39$, which is the value typically used. However, variations of $\pm 30\%$ could still explain most of our data. Unfortunately we are left with one additional empirical parameter S_q , which could be tested only in the overall agreement of the modeled and observed temperature field.

The surface mixing length inferred from our data is much less than previous estimates. [Craig's \(1996\)](#) laboratory measurements and the field experiments of [Drennan et al. \(1996\)](#) and [Terray et al. \(1996\)](#) found values of z_0 comparable to the significant wave height and scaling with the wave length of the dominant waves. However, these larger values of the surface mixing length are based on matching the turbulence model to dissipation measurements. The modeled dissipation profile depends strongly on the choice of the empirical constant S_q . By adjusting S_q it might be possible to reconcile diffusivity and dissipation profiles with the much smaller value of z_0 found here. However, this large discrepancy is puzzling and there is need for further independent estimates of z_0 together with simultaneous measurements of dissipation.

Although turbulence, generated by wave breaking and shear-driven overturns, and the advective flow field of Langmuir circulation can be separated for this calculation, any interpretation of the near-surface temperature field has to combine both components. Our analysis implies that close to the surface transport of heat occurs mainly through turbulent diffusion, but advection dominates at depths ≥ 0.5 m.

Our interpretation of near-surface turbulence has been one-dimensional, whereas the transport of heat has been interpreted as two-dimensional. This simplification was justified on the basis that timescales associated with turbulence and advection due to wave breaking and shear flow instability were short compared to the timescale of Langmuir circulation. The temperature field is affected by more persistent advective effects which must therefore be included in the analysis of temperature–depth time series. While such finely resolved descriptions of the ocean surface layer are unsuitable for direct inclusion in larger-scale studies where the detailed dynamics is of less interest (e.g., [Large et al. 1994](#)), combined models of near-surface turbulence and Langmuir circulation are required for interpretation of bubble distributions and calculation of bubble-enhanced air–sea gas flux, as well as plankton distributions and the vertical transport of oil and other contaminants (cf. [Farmer and Li 1994](#)). More generally, better descriptions of small-scale structure near the ocean surface will contribute to improved model representation of subgrid-scale processes.

[Thorpe \(1984b\)](#) has proposed use of bubble size distributions for the purpose of evaluating turbulent diffusion; this

requires inclusion of buoyancy and dissolution effects and would more properly be carried out using measurements of the bubble size spectrum as a function of depth and time. Interpretation of near-surface turbulence in terms of combined measurements of temperature and bubble size distribution remains a longer-term goal. In this context, unambiguous separation of bubble injections induced by breaking waves from the effects of Langmuir convergence will be especially important.

Comparison between modeled dissipation within the mixed layer and energy input into the wave field shows that breaking waves are the major source of turbulent kinetic energy in the wind-driven surface layer. In this time-averaged description a maximum dissipation enhancement of approximately ten times the dissipation rate expected in a constant stress layer is predicted close to the surface. A constant stress layer or depth-independent parameterization of turbulent diffusion (cf. [Li and Garrett 1995](#)) is not consistent with our observations. “Wall layer” coordinates do not collapse our different datasets and, as pointed out by [Drennan et al. \(1992\)](#), are inappropriate in this environment.

Application of a two-dimensional advection–diffusion model with the turbulence characteristics defined above may allow determination of the strength and size of Langmuir circulation, based only on accurate temperature measurements within the top few meters and knowledge of the air–sea heat flux. The model implies that it would be difficult to detect a temperature signal associated with Langmuir circulation below approximately half the cell depth.

Although our dataset is limited to an eight-hour deployment at nighttime and relatively high wind speeds, more extended observations of near-surface bubble clouds show the presence of Langmuir circulation throughout most of the higher sea states encountered during the Marine Boundary Layer experiment, regardless of the sign of the air–sea heat flux. Wave breaking is a function of the wind, wave, and current field, and therefore we expect the turbulence characteristics described above to be applicable to periods with solar radiation. However, absorption of shortwave radiation in the ocean is distributed over several meters and for daylight observations the model [equations \(2\) and \(4\)](#) need to include the depth dependence of the heat flux.

Acknowledgments

This work was made possible with the help of technical staff of the acoustical oceanography group at the Institute of Ocean Sciences and support of the U.S. Office of Naval Research through the Marine Boundary Layer program. We are indebted to the crew of R/V *Wecoma* for assistance in deployment and recovery of the instrumentation. Dr. J. Edson provided the surface heat flux, V. Polonichko prepared the sidescan and sonar images, and Dr. P. Craig supplied the code for the turbulence closure model. The mixed layer floats were deployed in collaboration with Dr. E. D’Asaro and G. Dairiki; D. Veenstra assisted with the processing. We thank Drs. C. Garrett, R. Lueck, and J. Moum for helpful discussions and the reviewers for their constructive comments.

REFERENCES

- Agrawal, Y. C., E. A. Terray, M. A. Donelan, P. A. Hwang, A. J. Williams III, W. M. Drennan, K. K. Kahma, and S. A. Kitaigorodskii, 1992: Enhanced dissipation of kinetic energy beneath surface waves. *Nature*, **359**, 219–220.
- Anis, A., and J. N. Moum, 1992: The superadiabatic surface layer of the ocean during convection. *J. Phys. Oceanogr.*, **22**, 1221–1227. [Find this article online](#)
- , and —, 1995: Surface wave–turbulence interactions: Scaling $\epsilon(z)$ near the sea surface. *J. Phys. Oceanogr.*, **25**, 2025–2045. [Find this article online](#)
- Craig, P. D., 1996: Velocity profile and surface roughness under breaking waves. *J. Geophys. Res.*, **101**, 1265–1277.
- , and M. L. Banner, 1994: Modeling wave-enhanced turbulence in the ocean surface layer. *J. Phys. Oceanogr.*, **24**, 2546–2559. [Find this article online](#)
- D’Asaro, E. A., and G. T. Dairiki, 1997: Turbulence intensity measurements in a wind-driven mixed layer. *J. Phys. Oceanogr.*, **27**, 2009–2022. [Find this article online](#)
- Drennan, W. M., K. K. Kahma, E. A. Terray, M. A. Donelan, and S. A. Kitaigorodskii, 1992: Observations of the enhancement of kinetic energy dissipation beneath breaking wind waves. *Breaking Waves IUTAM Symposium*, M. L. Banner and R. H. J. Grimshaw, Eds., Springer-Verlag, 95–101.
- , M. A. Donelan, E. A. Terray, and K. B. Katsaros, 1996: Oceanic turbulence measurements in SWADE. *J. Phys. Oceanogr.*, **26**, 808–815. [Find this article online](#)

Efron, B., and G. Gong, 1983: A leisurely look at bootstrap, the jackknife, and cross-validation. *Amer. Stat.*, **37**, 36–48..

Farmer, D., and M. Li, 1994: Oil dispersion by turbulence and coherent circulation. *Ocean Eng.*, **21** (6), 575–586..

—, and —, 1995: Patterns of bubble clouds organized by Langmuir circulation. *J. Phys. Oceanogr.*, **25**, 1426–1440.. [Find this article online](#)

—, and J. R. Gemmrich, 1996: Measurements of temperature fluctuations in breaking surface waves. *J. Phys. Oceanogr.*, **26**, 816–825.. [Find this article online](#)

—, —, and V. Polonichko, 1998: Velocity, temperature and spatial structure of Langmuir circulation. *Physical Processes in Lakes and Oceans*, J. Imberger, Ed., *Coastal and Estuary Studies*, Vol. 54, Amer. Geophys. Union..

Frost, W., and T. H. Moulden, 1977: *Handbook of Turbulence*, Vol. 1. Plenum Press, 498 pp..

Gemmrich, J. R., 1997: A study of turbulence and fine scale temperature variability of the ocean thermal boundary layer under breaking surface waves. Ph.D. thesis, University of Victoria, Victoria, BC, Canada, 209 pp..

—, T. D. Mudge, and V. D. Polonichko, 1994: On the energy input from wind to surface waves. *J. Phys. Oceanogr.*, **24**, 2413–2417.. [Find this article online](#)

Hasse, L., 1971: The sea surface temperature deviation and the heat flow at the sea–air interface. *Bound.-Layer Meteor.*, **1**, 368–379.

Jessup, A. T., 1996: The infrared signature of breaking waves. *The Air–Sea Interface*, M. A. Donelan, W. H. Hui, and W. J. Plant, Eds., University of Toronto Press, 665–670..

Katsaros, K. B., 1980: The aqueous thermal boundary layer. *Bound.-Layer Meteor.*, **18**, 107–127..

Kitaigorodskii, S. A., 1984: On the fluid dynamical theory of turbulent gas transfer across an air–sea interface in the presence of breaking waves. *J. Phys. Oceanogr.*, **14**, 960–972.. [Find this article online](#)

Kundu, P. K., 1990: *Fluid Mechanics*. Academic Press, 638 pp..

Large, W. G., J. C. McWilliams, and S. C. Doney, 1994: Oceanic vertical mixing: A review and a model with a nonlocal boundary layer parameterization. *Rev. Geophys.*, **32**, 363–403..

Li, M., and C. Garrett, 1995: Is Langmuir circulation driven by surface waves or surface cooling? *J. Phys. Oceanogr.*, **25**, 64–76.. [Find this article online](#)

Mellor, G. L., and T. Yamada, 1982: Development of a turbulent closure model for geophysical fluid problems. *Rev. Geophys. Space Phys.*, **20**, 851–875..

Mudge, T. D., and R. G. Lueck, 1994: Digital signal processing to enhance oceanographic observations. *J. Atmos. Oceanic Technol.*, **11**, 825–835..

Myer, G. E., 1969: A field study of Langmuir circulations. *Proc. 12th Conf. on Great Lakes Research*, Ann Arbor, MI, Int. Assoc. for Great Lakes Res., 652–663..

Osborn, T., D. M. Farmer, S. Vagle, S. A. Thorpe, and M. Cure, 1992: Measurements of bubble plumes and turbulence from a submarine. *Atmos.–Ocean*, **30**, 419–440..

Polonichko, V. D., 1997: Response of the upper ocean to wind, wave and buoyancy forcing. Ph.D. thesis, University of Victoria, Victoria, BC, Canada..

Prandtl, L., 1925: Bericht über Untersuchungen zur ausgebildeten Turbulenz. *Z. angewandte Math. Mech.*, **5**, 136–139..

Rapp, R. J., and W. K. Melville, 1990: Laboratory measurements of deep-water breaking waves. *Philos. Trans. Roy. Soc. London, Ser. A*, **331**, 731–800..

Schlüssel, P., W. J. Emery, H. Graßl, and T. Mammen, 1990: On the bulk skin temperature difference and its impact on satellite remote sensing of sea surface temperature. *J. Geophys. Res.*, **95**, 13 341–13 356..

Terray, E. A., M. A. Donelan, Y. C. Agrawal, W. M. Drennan, K. K. Kahma, A. J. Williams III, P. A. Hwang, and S. A. Kitaigorodskii, 1996: Estimates of kinetic energy dissipation under breaking waves. *J. Phys. Oceanogr.*, **26**, 792–807.. [Find this article online](#)

Terrill, E., and W. K. Melville, 1997: Sound speed measurements in the surface-wave layer. *J. Acoust. Soc. Amer.*, **102**, 1–19..

Thorpe, S. A., 1984a: The effect of Langmuir circulation on the distribution of submerged bubbles caused by breaking wind waves. *J. Fluid Mech.*, **142**, 151–170..

— ,1984b: A model of the turbulent diffusion of bubble clouds below the sea surface. *J. Phys. Oceanogr.*, **14**, 841–854.. [Find this article online](#)

— ,1992: Bubble clouds and the dynamics of the upper ocean. *Quart. J. Roy. Meteor. Soc.*, **118**, 1–22..

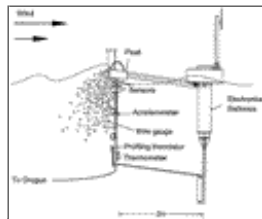
— ,1995: Dynamical processes of transfer at the sea surface. *Progress in Oceanography*, Vol. 35, Pergamon, 315–352..

— ,and A. J. Hall, 1982: Observations of the thermal structure of Langmuir circulation. *J. Fluid Mech.*, **114**, 237–250..

— ,and — ,1987: Bubble clouds and temperature anomalies in the upper ocean. *Nature*, **328**, 48–51..

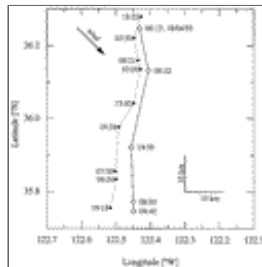
Woolf, D. K., and S. A. Thorpe, 1991: Bubbles and the air–sea exchange of gases in near saturation conditions. *J. Mar. Res.*, **49**, 435–466..

Figures



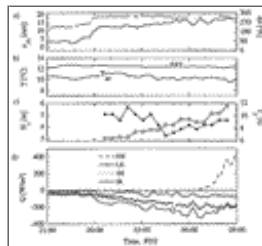
[Click on thumbnail for full-sized image.](#)

Fig. 1. Self-contained instrument for measurement of breaking waves and surface layer thermal processes. The profiling thermistor acquires temperature measurements from 1.8 m up to the air–sea interface at 60-s intervals.



[Click on thumbnail for full-sized image.](#)

Fig. 2. ARGOS position of the surface drifter (solid line) and the instrument monitoring the near-surface bubble field (dotted line) during 18–19 Apr 1995. Times are in PDT.



[Click on thumbnail for full-sized image.](#)

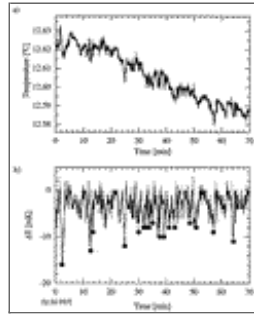
Fig. 3. Environmental conditions during the 18 Apr 1995 deployment. (a) Wind speed corrected to 10-m height (line) and wind direction (circles); (b) air temperature and sea surface temperature; (c) significant wave height (open) and peak wave period (solid); and (d) air–sea heat flux components: total solar radiation SW (dashed), net infrared radiation (IR) (open circles), sensible heat flux (SH) (dots), latent heat flux (LE) (solid circles), and total heat flux within the thermal boundary layer Q (solid line).





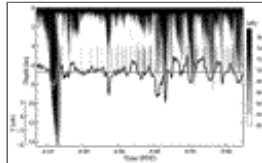
[Click on thumbnail for full-sized image.](#)

Fig. 4. Scanning sonar image showing bubble cloud distributions at 0407:59 PDT 18 Apr 1995, Dark bands are bubble clouds organized by Langmuir circulation. Small arrow depicts wind direction (courtesy V. Polonichko). Long arrow indicates drift of the temperature profiling instrument relative to the drifting bubble cloud pattern.



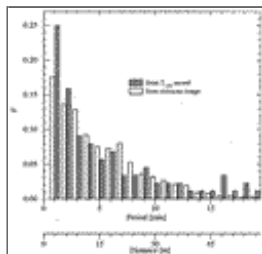
[Click on thumbnail for full-sized image.](#)

Fig. 5. (a) Temperature record at 1.8-m depth starting at 0230 PDT 18 Apr 1995. (b) Maximum temperature deviation within previous 60 s (line) illustrating detection scheme of temperature events and detected temperature events (circle) [same time interval as in (a)].



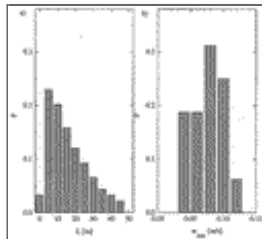
[Click on thumbnail for full-sized image.](#)

Fig. 6. Backscatter intensity detected with a vertically oriented sonar (198 kHz) and time series of the temperature deviation at 6.5-m depth (courtesy of V. Polonichko).



[Click on thumbnail for full-sized image.](#)

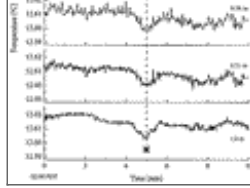
Fig. 7. Distribution of time periods between (a) (gray bars) successive temperature events and (b) (open bars) a simulation of the probability distribution for Langmuir convergence crossing based on simultaneously acquired imaging sonar data and satellite tracking of the profiling thermistor instrument. The lower axis indicates distances based on a mean instrument drift speed of 0.05 m s^{-1} .



[Click on thumbnail for full-sized image.](#)

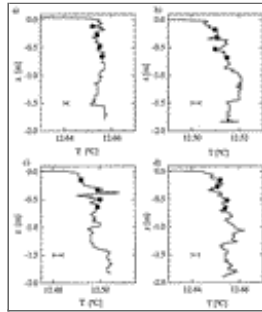
Fig. 8. Distribution of (a) cell width and (b) downwelling velocities coinciding with temperature measurements.





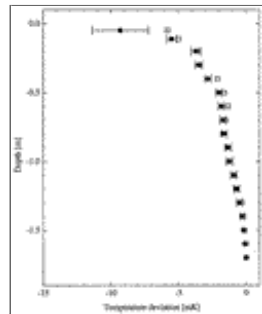
[Click on thumbnail for full-sized image.](#)

Fig. 9. Temperature at five depths showing temperature fluctuation (*- -*) associated with Langmuir convergence zones.



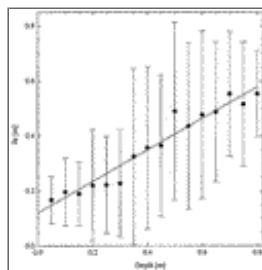
[Click on thumbnail for full-sized image.](#)

Fig. 10. Representative near-surface temperature profiles (line) on 18 Apr 1995 at (a) 0033, (b) 0403, (c) 0448, and (d) 0607 PDT. Dots give temperatures recorded with fixed depth thermistors. Horizontal bars depict one standard deviation of the temperature record within the water column. The depth is referenced to the instantaneous surface detected via the capacitance wire gauge.



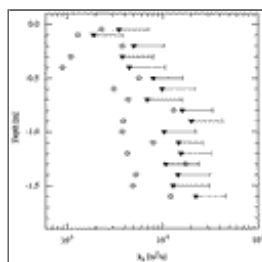
[Click on thumbnail for full-sized image.](#)

Fig. 11. Average temperature profile during 18 Apr 1995 deployment, expressed as deviation from mean value within the deepest 0.1-m bin. Prior to averaging the profiles were subsampled to 0.1-m steps.



[Click on thumbnail for full-sized image.](#)

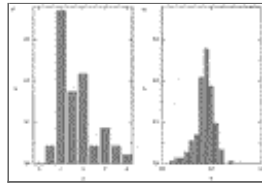
Fig. 12. Mean values of vertical extension of temperature disturbances, obtained from 1000 bootstrap iterations and a linear fit. Error bars represent one standard deviation.



[Click on thumbnail for full-sized image.](#)

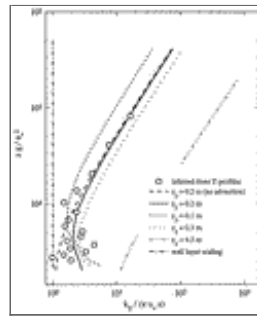
Fig. 13. Profiles of apparent turbulent diffusivity inferred from temperature profiles in the vicinity of Langmuir convergence

zones (open circles) and between convergences (triangles). Error bars represent absolute standard error $\sigma/(n)^{1/2}$, where σ is the standard deviation and n the number of individual profiles.



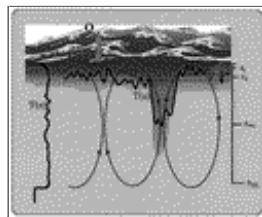
[Click on thumbnail for full-sized image.](#)

Fig. 14. Distribution of (a) cell aspect ratio and (b) cell asymmetry acquired in Jan 1995.



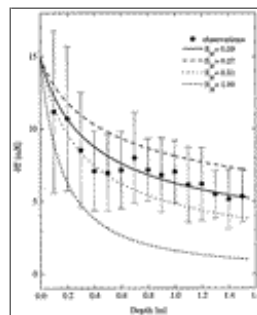
[Click on thumbnail for full-sized image.](#)

Fig. 15. Comparison between observations and modeled turbulent diffusivity profiles.



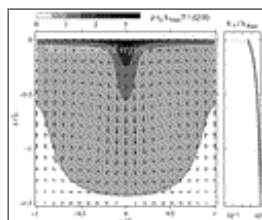
[Click on thumbnail for full-sized image.](#)

Fig. 16. Sketch of processes relevant for near-surface temperature fine structure. The relevant depth scales are mixed layer depth z_{ML} , depth z_{we} of wave-enhanced turbulence, depth z_0 of whitecap penetration, and depth of boundary layer of anomalous temperature z_t . The cool skin is not resolved in this drawing.



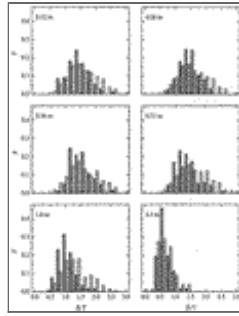
[Click on thumbnail for full-sized image.](#)

Fig. 17. Mean values of observed magnitude of temperature disturbances, obtained from 1000 bootstrap iterations. Error bars represent one standard deviation. Lines show modeled temperature anomalies for different values of S_M .



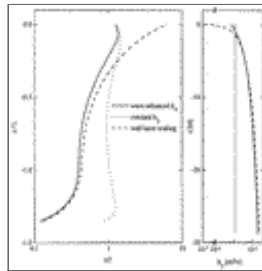
[Click on thumbnail for full-sized image.](#)

Fig. 18. Modeled temperature and velocity field ($L = 20$ m, $\alpha = 0.4$, $\gamma = 1.5$, $u_{\max} = 0.08$ m s⁻¹). The selected diffusivity profile (right panel) is obtained from a modified [Craig and Banner \(1994\)](#) model for $z_0 = 0.2$. The constant stress layer scaling is shown by a dashed line.



[Click on thumbnail for full-sized image.](#)

Fig. 19. Distribution of observed (solid) and modeled (pattern) temperature fluctuations at all sensor depths.



[Click on thumbnail for full-sized image.](#)

Fig. 20. Left: Profile of temperature difference between upwelling and downwelling regions of modeled temperature fields for (a) wave-enhanced turbulence near the surface (solid), (b) depth-independent diffusivity (dots), and (c) constant stress layer scaling (dashes). Right: Corresponding diffusivity profiles. (Note axis break to accommodate the low constant stress layer diffusivities close to the surface.)

Corresponding author address: Dr. David M. Farmer, Institute of Ocean Sciences, Post Office Box 6000, Sidney, BC V8L 4B2, Canada.

E-mail: farmerd@dfo-mpo.gc.ca

[top ▲](#)



© 2008 American Meteorological Society [Privacy Policy and Disclaimer](#)
 Headquarters: 45 Beacon Street Boston, MA 02108-3693
 DC Office: 1120 G Street, NW, Suite 800 Washington DC, 20005-3826
amsinfo@ametsoc.org Phone: 617-227-2425 Fax: 617-742-8718
[Allen Press, Inc.](#) assists in the online publication of AMS journals.